Astronomy & Astrophysics

Tests of stellar model atmospheres by optical interferometry

III. NPOI and VINCI interferometry of the M0 giant γ Sagittae covering 0.5–2.2 μm[⋆],[⋆⋆]

M. Wittkowski[1], C. A. Hummel[2], J. P. Aufdenberg[3], and V. Roccatagliata[4]

[1] European Southern Observatory, Karl-Schwarzschild-Str. 2, 85748 Garching bei München, Germany
    e-mail: mwittkow@eso.org
[2] European Southern Observatory, Casilla 19001, Santiago 19, Chile
[3] National Optical Astronomy Observatory, 950 North Cherry Avenue, Tucson, AZ 85719, USA
[4] Max-Planck-Institut für Astronomie, Königsstuhl 17, 69117 Heidelberg, Germany

ABSTRACT

Context. Optical interferometry allows a measurement of the intensity profile across a stellar disc, leading to a direct test and calibration of theoretical model atmospheres as well as to a precise determination of fundamental stellar parameters.

Aims. We present a comparison of the visual and near-infrared intensity profile of the M0 giant γ Sagittae to plane-parallel `ATLAS 9` as well as to plane-parallel and spherical `PHOENIX` model atmospheres.

Methods. We use previously described visual interferometric data obtained with the Navy Prototype Optical Interferometer (NPOI) in July 2000. We apply the recently developed technique of *coherent integration*, and thereby obtain visibility data of more spectral channels (526–852 nm) and with higher precision than before. In addition, we employ new measurements of the near-infrared K-band ($\sim$2200 nm) diameter of γ Sagittae obtained with the instrument VINCI at the ESO VLT Interferometer (VLTI) in 2002.

Results. The spherical `PHOENIX` model leads to a precise definition of the Rosseland angular diameter and a consistent high-precision diameter value for our NPOI and VLTI/VINCI data sets of $\Theta_{\rm Ross} = 6.06 \pm 0.02$ mas, with the Hipparcos parallax corresponding to $R_{\rm Ross} = 55 \pm 4\,R_\odot$, and with the bolometric flux corresponding to an effective temperature $T_{\rm eff} = 3805 \pm 55$ K. Our visual visibility data close to the first minimum and in the second lobe constrain the limb-darkening effect and are generally consistent with the model atmosphere predictions. The visual closure phases exhibit a smooth transition between 0 and π.

Conclusions. The agreement between the NPOI and VINCI diameter values increases the confidence in the model atmosphere predictions from optical to near-infrared wavelengths as well as in the calibration and accuracy of both interferometric facilities. The consistent night-by-night diameter values of VINCI give additional confidence in the given uncertainties. The closure phases suggest a slight deviation from circular symmetry, which may be due to surface features, an asymmetric extended layer, or a faint unknown companion.

Key words. techniques: interferometric – stars: late-type – stars: AGB and post-AGB – stars: fundamental parameters – stars: atmospheres – stars: individual: γ Sagittae

1. Introduction

Cool giants on the red giant branch (RGB) and asymptotic giant branch (AGB) are very luminous and extended, have a low surface temperature, and their atmospheres can thus be rich in molecules. Cool giants are the most important source of dust formation and its delivery to the interstellar medium. The detailed structure of their extended atmospheres, including the effects from circumstellar molecular and dust layers, are still a matter of investigation and debate (cf., e.g. Scholz 1985, 1998, 2001; Perrin et al. 2004; Ohnaka 2004a; Ireland & Scholz 2006).

⋆ Based on data obtained with the Navy Prototype Optical Interferometer (NPOI). The NPOI is a joint project of the Naval Research Laboratory and the United States Naval Observatory in cooperation with Lowell Observatory, and is funded by the Office of Naval Research and the Oceanographer of the Navy.

⋆⋆ Based on public commissioning data released by the Paranal Observatory, Chile, and received via the ESO/ST-ECF Science Archive Facility.

Theoretical atmosphere models predict in general the spectrum emerging from every point of a stellar disc. Optical interferometry provides the strongest observational constraint of this prediction by resolving the stellar disc. In addition, the constraints on the intensity profiles allow us to find meaningful definitions of the stellar radius and its precise measurement.

For regular cool non-pulsating giants, the centre-to-limb variation (CLV) is mainly characterised by the limb-darkening effect, which is an effect of the vertical temperature profile of the stellar atmosphere. The strength of the limb-darkening can be probed by optical interferometry in two ways (cf., e.g. Hanbury Brown et al. 1974; Quirrenbach et al. 1996; Burns et al. 1997; Hajian et al. 1998; Wittkowski et al. 2001, 2004; Aufdenberg et al. 2005): (1) by measuring variations of an equivalent uniform disc diameter (i.e. the uniform disc that has the same integral flux as the true intensity profile) as a function of wavelength, and (2) by directly constraining the star's intensity profile in the second and higher lobes of the visibility function at one or several bandpasses.

It was found that pulsating giants as well as supergiants may exhibit more complex intensity profiles at near- and mid-infrared wavelengths, showing Gaussian-shaped intensity profiles, tail-like extensions to a photospheric intensity profile, and multiple components, such as a photosphere plus a circumstellar shell (cf., e.g. Woodruff et al. 2004; Ohnaka 2004a,b; Perrin et al. 2004, 2005; Fedele et al. 2005). Additionally, observed intensity profiles might be affected by dust shells (e.g. Ohnaka et al. 2005; Ireland & Scholz 2006) or horizontal surface inhomogeneities (e.g. Burns et al. 1997).

In Wittkowski et al. (2001, hereafter Paper I), we used the Navy Prototype Optical Interferometer (NPOI, Armstrong et al. 1998), used the method of baseline bootstrapping (cf. Hajian et al. 1998), and developed improved methods of compensation of noise and detection bias terms, in order to obtain precise visual visibility measurements in the second lobe of the visibility function for three cool giants. We found agreement with predictions by plane-parallel ATLAS 9 (1993) model atmospheres within the obtained wavelength range and precision. Thereby, the strength of the limb-darkening effect and the stars' fundamental parameters were constrained. Aufdenberg & Hauschildt (2003) compared one of the NPOI observations of γ Sagittae from Paper I to a spherical PHOENIX (1999) model atmosphere and found agreement. In Wittkowski et al. (2004, hereafter Paper II), we directly measured the limb-darkening effect of the M4 giant ψ Phoenicis using the ESO Very Large Telescope Interferometer (VLTI) in the near-infrared K-band, confronted the observations with predictions by independently constructed ATLAS 9 and PHOENIX model atmospheres, and found agreement with all considered models.

Recently, Hummel et al. (2003) developed the method of *coherent integration* and its application to NPOI data in order to increase the precision of visibility measurements. This method was recently applied by Peterson et al. (2006a,b) to NPOI observations of Altair and Vega.

Here, we reanalyse the NPOI data of the M0 giant γ Sagittae (HR 7635, HD 189319), the brightest of the targets in Paper I, using the newly developed method of *coherent integration*. We obtain visibility data with higher precision than in Paper I, and – due to the lower noise – are able to make use of more spectral channels toward the blue end of NPOI's wavelength range. Now, the wider wavelength range covers 526–852 nm, compared to 649–852 nm in Paper I. We thus also increase our maximum spatial resolution from ≈3.3 mas to ≈2.7 mas, which gives important additional visibility data in the second lobe that are sensitive to the limb-darkening effect. In addition, we observed γ Sagittae with the ESO Very Large Telescope Interferometer (VLTI) and its K-band instrument VINCI, in order to compare results derived from different interferometric facilities, and to probe the consistency of the wavelength-independent Rosseland diameter from visual to near-infrared wavelengths.

The cool giant γ Sagittae does not appear in the Combined General Catalogue of Variable Stars (Samus et al. 2004), indicating that it lacks strong photometric variability. Thus, it is a good target for the purpose of calibrating model atmospheres and deriving high-precision fundamental parameters. The spectral type has been listed as K5-M0 III by Morgan & Keenan (1973), and been revised to M0 III by Keenan & McNeil (1989). Wisniewski & Morrison (private communication) confirm by means of optical echelle spectra recently obtained at Ritter Observatory that γ Sagittae's spectrum closely resembles that of the MK standard μ UMa (M0 III). We determine the bolometric flux of γ Sagittae to $f_{bol} = (2.57 \pm 0.13) \times 10^{-9}$ W/m^2 by means of a spline fit and integration of the narrow-band

spectrophotometric data by Alekseeva et al. (1997) covering 405 nm to 1080 nm complemented by broadband photometry shortward and longward of this range from the 13-colour photometry by Johnson et al. (1975). The values for f_{bol} of $(2.79 \pm 0.14) \times 10^{-9}$ W/m^2 and $(2.83 \pm 0.14) \times 10^{-9}$ W/m^2 by Alonso et al. (1999) and Mozurkewich et al. (2003), respectively, are derived from broad-band photometry alone and likely overestimate f_{bol} because of a too sparse sampling of the visual spectrum including the TiO band heads and other features. The limb-darkened angular diameter of γ Sagittae has been determined in Paper I to be 6.18 ± 0.07 mas, based on a comparison of NPOI visibility data to ATLAS 9 model atmospheres. This value corresponds to a limb-darkened radius of 56 ± 4 $R_{\odot}$, derived with the Hipparcos parallax of 11.90 ± 0.71 mas (Perryman & ESA 1997). These values of angular diameter, absolute radius, and bolometric flux constrain the effective temperature to $T_{eff} = 3768$ K ± 70 K, and the luminosity to $\log L/L_{\odot} = 2.75 \pm 0.10$. Placing γ Sagittae on the Hertzsprung Russel diagram using these values, and comparing to stellar evolutionary tracks by Girardi et al. (2000) as in Paper II (Fig. 1 of Paper II) we can estimate a mass of $M = 1.3 \pm 0.4 M_{\odot}$, and thus a surface gravity of $\log g = 1.06 \pm 0.22$. These values are used as an a priori estimate for our analysis and will be refined in the conclusions.

2. NPOI measurements

2.1. NPOI observations

We reanalyse the visual γ Sagittae data in Paper I obtained with NPOI on July 21, 2000. The centre (C), east (E) and west (W) siderostats of the astrometric sub-array of NPOI were used to obtain baselines of ground length 18.9 m (CE), 22.2 m (CW), and 37.5 m (EW). The data were recorded in 32 spectral channels of equal width in wavenumber and covering the band from ≈450 nm to 850 nm. Due to low photon count rates only the 10 reddest channels could be used in Paper I (covering 649 nm to 852 nm). We reanalyse the same raw data using the newly developed coherent integration algorithm as first described by Hummel et al. (2003). The details of our new analysis are described below. The benefits of the new analysis include an improved signal-to-noise-ratio (*SNR*) of the visibility data on the long EW baseline, as well as a much improved *SNR* of the triple amplitudes and phases. These improvements enable us to use the 20 reddest channels in the present paper, now covering 526 nm to 852 nm.

2.2. NPOI data reduction and calibration

Coherent integration. The NPOI detector configuration used for our data set (July 2000) sampled a single fringe of each two telescope interference pattern using 8 bins every 2 ms. This time interval is called the instrumental coherent (because it is phase preserving) integration time. Increasing this time would eventually lead to a complete loss of fringe contrast due to atmospheric fringe motion which is not perfectly compensated by an interferometer such as NPOI using the group delay method for fringe tracking.

Therefore, in the so-called incoherent analysis, as used in Paper I, the bin counts of each 2 ms sample would be Fourier transformed, and an unbiased estimate for the squared visibility amplitude derived as follows (see Shao et al. 1988):

$$|V|^2 \sim \frac{\langle X^2 + Y^2 - \sigma_I^2(N) \rangle}{\langle N \rangle^2}, \qquad (1)$$

where X and Y are the real and imaginary parts of the Fourier transform, respectively, and σ_I^2 is the variance of the intensity caused by photon and detection noise. In the case of pure Poisson noise σ_I^2 equals N, the total number of bin counts of each sample. In the case of NPOI, the data of which show non-Poisson noise due to afterpulsing of the APDs (avalanche photo diodes), the bias is estimated according to procedures described in Paper I (see also below the paragraph "Correction of noise and detection bias terms").

The signal to noise ratio *SNR* of the squared visibility estimator is as follows (Shao et al. 1988):

$$SNR(V^2) = \frac{1}{4}M^{1/2}NV^2\left[1 + \frac{1}{2}NV^2\right]^{-1/2}, \qquad (2)$$

where M is the number of samples averaged. One can see that by increasing the coherent integration time, i.e. increasing N, rather than increasing M a larger gain in *SNR* can be realised. This is true as long as NV^2 is much smaller than unity, otherwise nothing can be gained by a coherent average over an incoherent average. Here, we chose a coherent integration time of 200 ms which still results in $NV^2 > 5$ for photon rates of 10 per 2 ms at squared visibilities of about 0.005. Subsequently, the squared visibility was computed for the coherent samples, and then incoherently averaged in 2 s intervals. The complex triple products were computed from the coherent samples as well, but vector averaged to preserve the phase. Coherent integration for time intervals longer than the instrumental coherent integration time (we chose 200 ms) require the alignment of the complex visibilities, equivalent to removing the relative offsets between successive samples of the fringe. As described by Hummel et al. (2003), this can be done in the off-line data analysis by making use of the visibility phase derivative with wavenumber. This quantity, the so-called group delay, is zero for the white light fringe which is located at zero relative optical path length difference where the fringes of all colours interfere constructively.

For the observations described here on γ Sagittae, the importance of coherent integration follows from the very small visibility amplitudes measured on the long EW baseline since it samples the second lobe of the Fourier transform of the stellar disc brightness profile. This baseline is therefore most sensitive to stellar limb darkening, the focus of this work. While the low visibility amplitudes on this baseline would prevent a precise determination of the group delay, the following paragraph describes how to obtain this estimate in a different way.

Phase bootstrapping. A design feature of the NPOI array (Armstrong et al. 1998) is the ability to realise configurations which allow long baselines to be boot-strapped by shorter baselines. By this we mean the ability to track and observe fringes on long baselines even though the fringe contrast can be too low to allow detection of the fringes for tracking purposes. This is achieved by detecting and tracking fringes on the shorter baselines, and making use of the fact that the sum of all fringe delays over baselines in a closed loop must equal zero.

In the case described here, the EW baseline is boot-strapped by the CE and CW baselines. Therefore, the fringe delay on the EW baseline is equal to the difference of the delay between the other two baselines, and can thus be computed in this way without using the measurement on the EW baseline itself.

Correction of noise and detection bias terms. As shown in Paper I, the standard correction for non-Poisson statistics of the
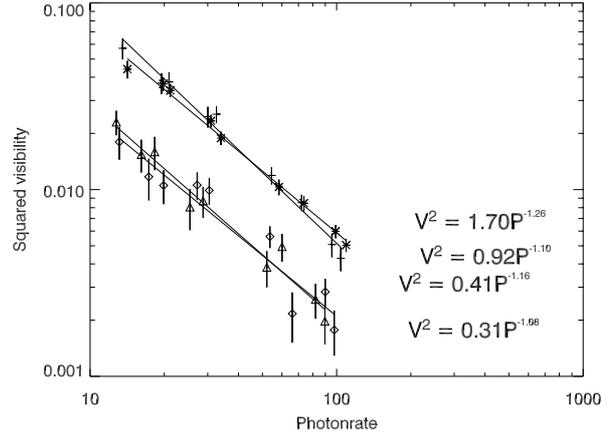
Fig. 1. Incoherent integration. Off-fringe squared visibility amplitude, i.e. the visibility bias that remains for data off the fringe packet and that is compensated after the Z^2 compensation (see text for more details). This bias can be described by a power law as a function of photon rate P. As an example, the residual bias is shown for the four reddest channels on the EW baseline. Data are 2 ms incoherent integrations from July 22. Channels 1 though 4 use symbols plus, star, diamond, and triangle, respectively. Power-law fit coefficients are given for each channel, in the same order as shown on the corresponding plot for the coherent analysis in Fig. 2.

NPOI detectors used by Hummel et al. (1998) (for σ_I^2 of Eq. (1), use Z^2 with $Z = B_1 - B_2 + B_3 - B_4 + B_5 - B_6 + B_7 - B_8$, where B_i are the bin counts) can be improved by compensating a small residual bias that remains after the Z^2 compensation. This residual bias is calibrated by a power law as a function of counts by observing off the fringe for a number of stars of different brightness (cf. Eqs. (3) and (4) of Paper I). This additional bias correction is important because of the small visibility amplitudes measured on resolved stars, where a constant residual bias would strongly contribute to the visibility values. A welcome side effect of the coherent integration is that, because the number of photons counted in a coherent integration, N, increases, the ratio of the bias to the signal decreases. Therefore, at a count rate high enough, the remaining bias after the Z^2 compensation becomes negligible. Since we chose a coherent integration time of 200 ms, a measurable, though much smaller, residual bias than in Paper I remained. This residual bias was removed using exactly the same procedures as described in Sect. 3 of Paper I by reducing data obtained on July 22 during which off-fringe data were recorded. Figures 1 and 2 show as an example for the 4 reddest channels of the EW baseline the remaining bias after the Z^2 compensation, obtained for the incoherent analysis as used in Paper I (2 ms integrations) and for the coherent analysis used here (200 ms coherent integrations, and normalised to a 2 ms interval), respectively. It can be seen that the residual bias for the coherent analysis is clearly reduced compared to the incoherent average. This is an additional benefit of the method of coherent integration.

Calibration. The calibration of the data followed the same procedures as used in Paper I. The B6 giant ϵ Delphini, 12 degrees away and observed in an interleaved way during the same night, is used as the main calibration star. The diameter of ϵ Delphini is estimated to be 0.3 mas based on a calibration of the visual magnitude and $(R - I)$ colour index by Mozurkewich et al. (1991). As secondary calibrators we used ι^2 Cygni and π^2 Pegasi, both 32 degrees away from γ Sagittae. The calibration errors of
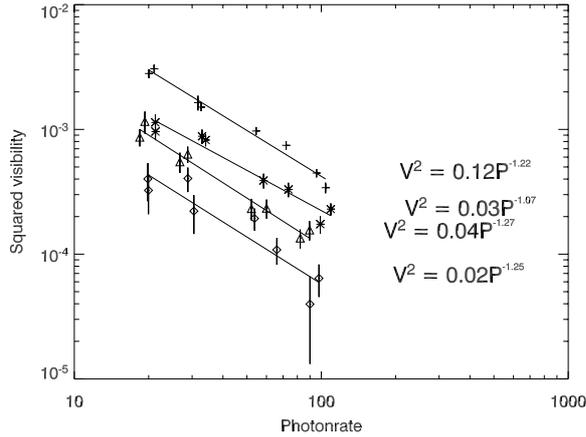
Fig. 2. Coherent integration. As Fig. 1, but for 200 ms coherent integrations as used in this paper. For reasons of comparison, the bin counts are renormalised to 2 ms intervals. It is an additional benefit of the coherent integration that this residual bias shown here is clearly reduced compared to the incoherent integration in Fig. 1.

the squared visibility amplitudes (derived from the scatter of the primary and secondary calibrator amplitudes and added in quadrature to the formal, i.e. photon noise induced errors) are now larger than those quoted in Paper I for the boot-strapped EW baseline, namely 13% versus 7%, while the calibration error for the other two baselines was only marginally larger. This is acceptable since the statistical errors dominate the total error budget for the EW baseline.

2.3. NPOI results

As a first characterisation of our NPOI data, we use models of a uniform disc (UD, $I = 1$ for $0 \leq \mu \leq 1$, $I = 0$ otherwise), and a fully darkened disc (FDD, $I = \mu$). Here, I is the intensity, $\mu = \cos\Theta$ (or $\mu = \sqrt{1 - (r/R)^2}$) the cosine of the angle between the line of sight and the normal of the surface element of the star (R the stellar radius, r the distance from the centre of the disc). Monochromatic synthetic visibility values V were obtained for the UD and FDD cases, and subsequently integrated over the bandpass of each NPOI spectral channel (covering frequencies ν_1 to ν_2) as

$$V_i = \frac{\int_{\nu_1}^{\nu_2} F_\nu V(\nu) \, d\nu}{\int_{\nu_1}^{\nu_2} F_\nu \, d\nu} \tag{3}$$

with F_ν the flux from the blackbody radiation. We use $T_{\text{eff}} = 3768$ K (see Sect. 1). Variations of T_{eff} within its uncertainties do not have a significant effect on the visibility values. Finally, the synthetic squared visibility values for each of the baselines ($|V_i(\text{CE})|^2$, $|V_i(\text{CW})|^2$, $|V_i(\text{EW})|^2$), the triple amplitude ($V_i^{\text{CEW}} = |V_i(\text{CE})\,V_i(\text{CW})\,V_i(\text{EW})|$), and the closure phase ($\Phi_i^{\text{CEW}} = 0$ if $V_i(\text{CE})\,V_i(\text{CW})\,V_i(\text{EW}) > 0$, $\Phi_i^{\text{CEW}} = \pi$ if $V_i(\text{CE})\,V_i(\text{CW})\,V_i(\text{EW}) < 0$) were obtained.

Note that in the case of NPOI the monochromatic visibility amplitudes are integrated before building the square, while for VLTI/VINCI the monochromatic *squared* visibility amplitudes are integrated (cf. Paper II). The reason for the difference is that the data processing of NPOI first integrates the photons on the APDs and the squared visibility is computed from the already integrated bin counts, while for VLTI/VINCI first the full powerspectrum is computed and integrated thereafter. This leads to

Table 1. Fit results of our NPOI data to models of a uniform disc (UD) and a fully darkened (FDD) disc. The formal errors of the diameter values are ~0.01 mas, additional calibration uncertainties are ~0.06 mas, total errors thus ~0.06 mas.

Model	Diameter	Parameter α	χ_ν^2
UD	$\Theta_{\text{UD}} = 5.64$ mas	$\alpha = 0$	11.0
FDD	$\Theta_{\text{FDD}} = 6.59$ mas	$\alpha = 1$	5.6

noticeable differences, in particular around the minima of the visibility function.

Best fitting angular diameters $\Theta_{\text{UD,FDD}}$ are derived from a least square optimisation. The resulting values are shown in Table 1 together with the reduced χ_ν^2 values. The number of degrees of freedom is 644 (7 observations times 19 spectral channels times (3 squared visibility plus 1 triple amplitude plus 1 closure phase), minus 21 values flagged for quality). The formal errors of the obtained diameter values are of the order of 0.01 mas, and are small compared to calibration uncertainties that are estimated to ~1% ~ 0.06 mas. Total errors are thus ~0.06 mas.

Figures 3–7 show the obtained NPOI squared visibility amplitudes on baselines EW, CE, CW, the NPOI triple amplitudes, and the NPOI closure phases, respectively. Also shown are the model atmosphere predictions as described below in Sect. 4.

The gain with respect to Paper I in the signal-to-noise ratio and in the number of usable spectral channels is thanks to the method of coherent integration, as can be seen by comparing these Figs. to the results based on incoherent averaging (Fig. 3 of Paper I).

The results (Figs. 3–7 and Table 1) show that the visual intensity profile of γ Sge is limb-darkened, clearly closer to a FDD model than to a UD model, while both of these simple descriptions do not provide a very good representation of our data. A detailed comparison of our visibility data to model atmosphere predictions is discussed below in Sect. 4.

## 3. VLTI/VINCI measurements

3.1. VLTI/VINCI observations

The near-infrared K-band interferometric data of γ Sagittae were obtained with the ESO Very Large Telescope Interferometer (VLTI, Glindemann et al. 2003), the instrument VINCI (Kervella et al. 2003), and the two VLTI test siderostats on June 28, July 8, July 11, July 15, August 8, September 12, and September 18, 2002. These data are public commissioning data released from the VLTI[1]. The VLTI stations E0 and G1 forming a ground baseline length of 66 m were used for all our observations. The observations were repeated during 7 different nights spread over more than 2 months in order to compute the night-to-night variation of the obtained diameter and thereby to estimate the calibration uncertainty caused by different atmospheric and possibly instrumental conditions. All data were obtained as series of typically 100 or 500 interferograms with a scan length of 250 μm and a fringe frequency of 295 Hz.

The stars 56 Aquilae and 31 Orionis were used as primary calibration stars and were observed in each of our observation nights close in time to the γ Sagittae observations. A number of additional calibration stars observed during these nights were used as secondary calibrators for γ Sagittae. The characteristics

---

[1] `http://www.eso.org/projects/vlti/instru/vinci/`
`vinci_data_sets.html`
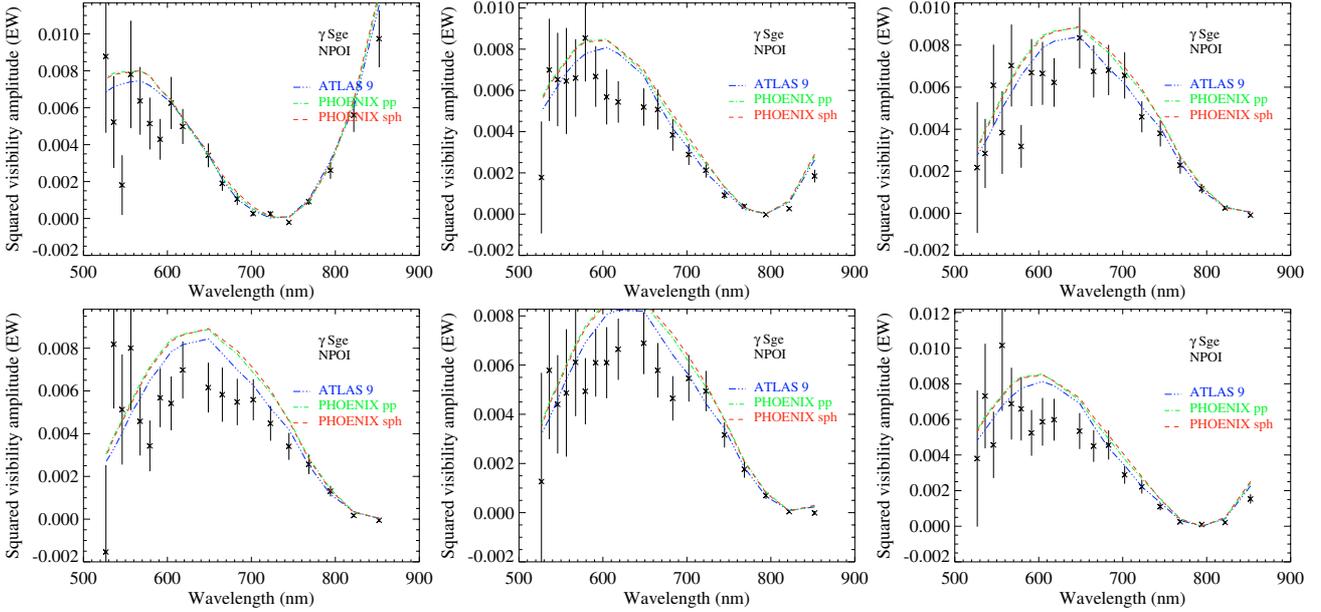
Fig. 3. Squared visibility amplitudes of γ Sge obtained from NPOI on the EW baseline. Also shown are synthetic visibility curves of the best fitting model atmospheres as described below in Sect. 4. Each model fit is performed to all NPOI visibility data (squared visibility amplitudes, triple amplitudes, and closure phases) simultaneously. The parameters of the plotted model curves are listed in Table 5. The synthetic visibility values are calculated for each specific bandpass of our observation and these points are connected by straight lines. A 7th used NPOI observation is not included for the sake of clarity of the figure and because its projected baseline length is much shorter and this observation thus contains little information in the 2nd lobe.
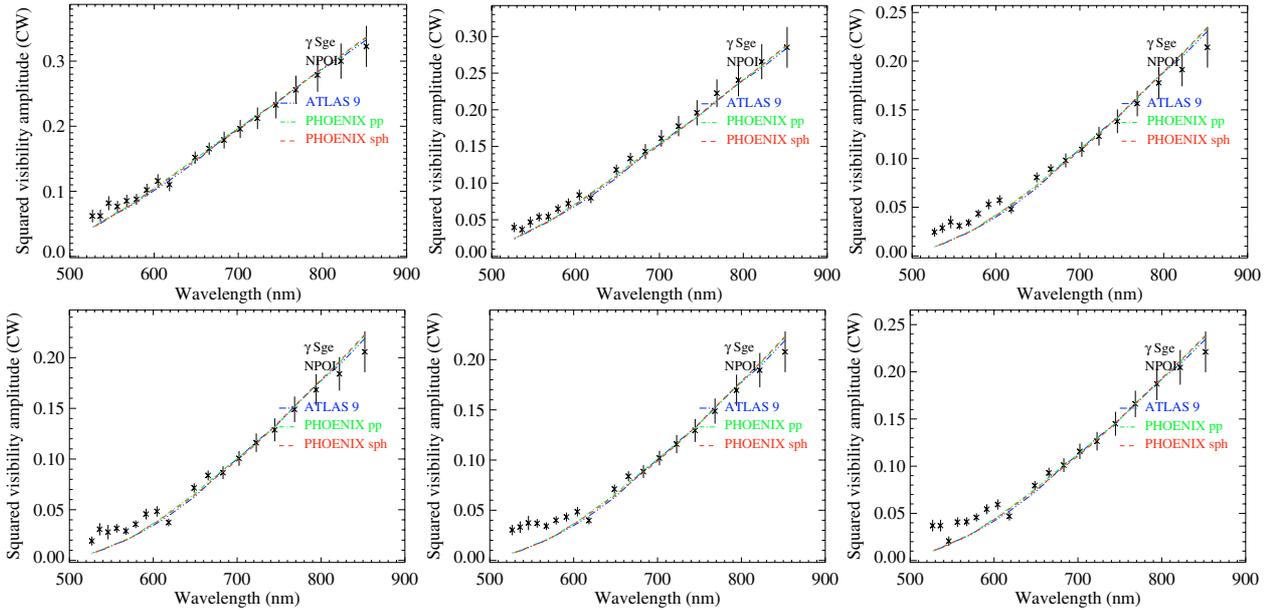
Fig. 4. As Fig. 3, but showing the squared visibility amplitudes on the NPOI CW baseline.

of all calibration stars used are taken from Bordé et al. (2002, based on Cohen et al. 1999) and are listed in Table 2.

3.2. VLTI/VINCI data reduction and calibration

We computed mean coherence factors for each series of interferograms using the VINCI data reduction software (version 3.0) by Kervella et al. (2004) employing the results based on the wavelets power spectral density. The calibration of the visibility values was performed as in Paper II using a weighted average of the transfer function values obtained during the night.

3.3. VLTI/VINCI results

Table 3 shows the observational details together with the resulting calibrated squared visibility amplitudes for each series of γ Sagittae interferograms. The listed errors include the scatter of the coherence factors of the single scans, the errors of the adopted diameter values of the calibration stars, and the variation of the obtained transfer function during each observing night.

As a first characterisation of the K-band stellar angular diameter, we compute the equivalent UD ($I = \mu^0$) and FDD ($I = \mu^1$) diameters, as for our NPOI data. The broad-band squared
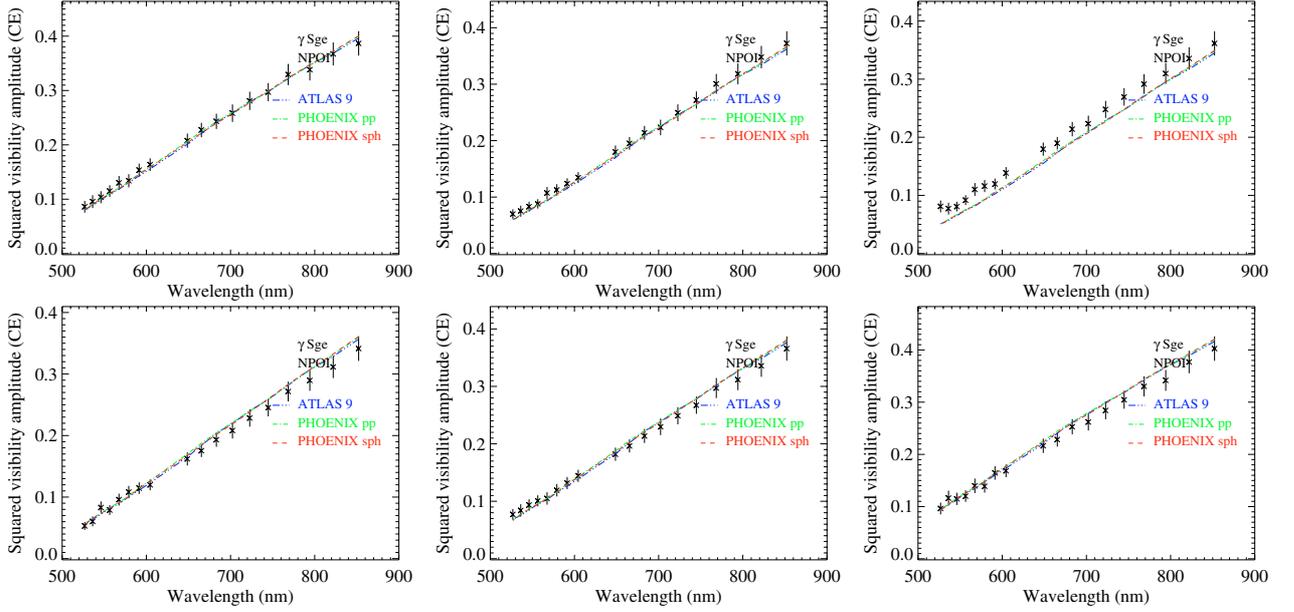
Fig. 5. As Fig. 3, but showing the squared visibility amplitudes on the NPOI CE baseline.
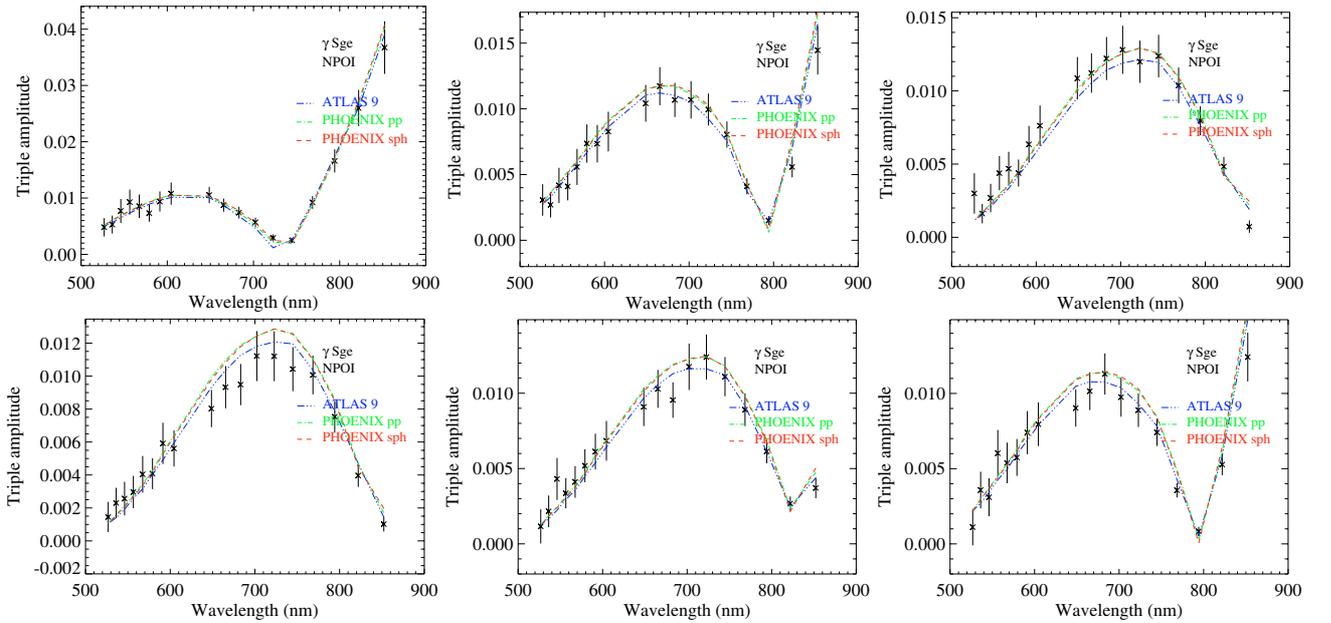
Fig. 6. As Fig. 3, but showing the NPOI triple amplitudes.

visibility amplitudes for the VINCI bandpass (*K*-band) are computed as

$$|V_K|^2 = \frac{\int_0^\infty F_\nu^2 S_\nu^2 |V(\nu)|^2 \, d\nu}{\int_0^\infty F_\nu^2 S_\nu^2 \, d\nu}, \tag{4}$$

where $V(\nu)$ is the monochromatic visibility, F_ν is the stellar flux (assumed as Planck radiation) and S_ν the VINCI sensitivity function including the transmission of the atmosphere, the optical fibers, the VINCI *K*-band filter, and the detector quantum efficiency.

Note that in the case of VLTI/VINCI the *squared* visibility amplitudes are integrated (Eq. (4)), while in the case of NPOI the visibility amplitudes have first to be integrated and squared thereafter (Eq. (3)), see the note in Sect. 2.3.

Table 4 lists the obtained diameter values for our VINCI data. Figure 8 shows our obtained VINCI squared visibility amplitudes of γ Sge together with the best-fitting models with parameters listed below in Table 5. Since our VINCI data cover only one bandpass and only data of the first lobe of the visibility function, it is – contrary to our NPOI data – not feasible to constrain the limb-darkening effect solely based on these VINCI data. This is also reflected by equal χ_ν^2 values obtained for UD and FDD models as well as by the virtually identical model visibility curves in Fig. 8.

The increased equivalent UD diameter with respect to the shorter NPOI wavelengths is consistent with the general trend of decreasing strength of the limb-darkening effect with increasing wavelength. A detailed comparison of our data to model atmospheres follows below in Sect. 4.
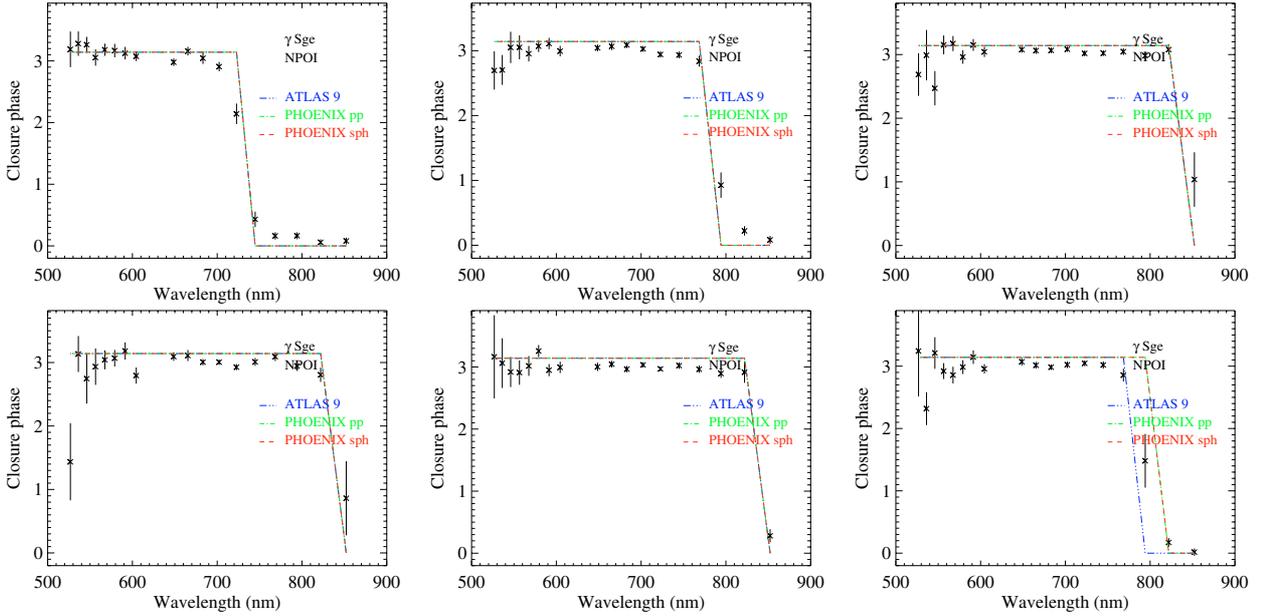
Fig. 7. As Fig. 3, but showing the NPOI closure phases. Note that the slope of the model flip from 0 to π is an artifact because the model values are only calculated for each NPOI spectral channel.

Analysis of calibration uncertainties. In order to test and verify the calibration uncertainties that are used in our analysis, we investigate the night-to-night variation of the obtained diameter values. All derived single nights' diameter values and uncertainties are consistent within 1.3σ with the value obtained from all data together (5.93 mas) as well as with the weighted mean of the single nights' values (5.92 mas).

This confirms that our diameter value is reliable and that our estimate of uncertainties is realistic. The obtained high-precision (0.3%) UD and FDD diameter values of $\Theta_{\text{UD}} = 5.93 \pm 0.02$ mas and $\Theta_{\text{FDD}} = 6.69 \pm 0.02$ mas can thus be used without further uncertainties.

Additional possible systematic errors that are constant over time scales larger than covered by our analysis, i.e. about 2 months, can not be ruled out. Such systematic errors could in principle be related to the calibration of the interferometric array and the instrument, such as the calibration of the baseline length or the effective wavelength. Such uncertainties are not expected to represent a considerable source of error.

4. Comparison to predictions by model atmospheres

4.1. Employed model atmospheres

We compare our measured visibility data to predictions by theoretical model atmospheres in order to calibrate and test these models, and to derive fundamental stellar parameters of γ Sge.

We use plane-parallel ATLAS 9 (Kurucz 1993) as well as plane-parallel and spherical PHOENIX (Hauschildt et al. 1999) model atmospheres to calculate synthetic visibility data, as done in Papers I and II. We refer to the descriptions in Papers I and II for more details on the employed model atmosphere files and their use. Differences between ATLAS 9 and PHOENIX models include different opacity tables, a different sampling of the model wavelengths, a different sampling of the angles (μ values), and convective overshooting that is taken into account for ATLAS 9, but not for PHOENIX.

The most important stellar input parameters for the plane-parallel models are effective temperature T_{eff} and surface gravity $\log g$, and for the spherical PHOENIX models in addition the mass M. We use solar chemical abundance, as appropriate for local cool giants. The values of T_{eff}, $\log g$, and M are already well constrained for γ Sagittae, as outlined in the Introduction (Sect. 1), namely $T_{\text{eff}} \sim 3768$ K, $\log g \sim 1.06$, $M \sim 1.3\,M_\odot$.

The closest model of the ATLAS 9 grid is the one for $T_{\text{eff}} = 3750$ K and $\log g = 1.0$ (see Papers I and II for details on the model file used). We have constructed a corresponding plane-parallel PHOENIX model atmosphere with parameters $T_{\text{eff}} = 3750$ K, $\log g = 1$, as well as a spherical PHOENIX model atmosphere with parameters $T_{\text{eff}} = 3750$ K, $\log g = 1.0$, and $M = 1.3$ (see Paper II for details on the model files).

4.2. Calculation of synthetic visibility data

We take into full account the bandpasses of our observations by integrating the synthetic visibility data of monochromatic intensity profiles for each spectral channel of NPOI and for the K-bandpass of VLTI/VINCI. This ensures that the synthetic visibility values fully resemble the true bandpasses used for the observations and that they include the model-predicted effects from atomic lines and molecular bands for each of our spectral channels. Monochromatic visibility values at frequency ν are calculated as (cf. Davis et al. 2000; Eq. (6) from Paper I; Eq. (1) from Paper II)

$$V_{\text{LD}}(\nu) = \int_0^1 (I_\nu(\mu)/I_\nu(0))\, J_0(\pi\, \Theta_{\text{LD}}\, (B/\lambda))\, \mu\, d\mu. \quad (5)$$

Here, $I_\nu(\mu)/I_\nu(0)$ is the normalised tabulated intensity profile, which is an output of the model atmosphere. J_0 is the Bessel function of first kind and order 0; Θ_{LD} is the limb-darkened angular diameter at which the intensity profile reaches 0; B is the projected baseline length. Note that the evaluation of this integral is vulnerable to numerical artifacts. We chose to use a linear interpolation of the irregularly tabulated $I(\mu)$ model values onto a regular grid of 1000 μ values between 0 and 1. The evaluation

Table 2. Characteristics of the stars that were used as calibration stars for our VLTI/VINCI observations of γ Sagittae. Listed are the spectral type, the *K*-band magnitude, the uniform-disc diameter and its error, and the effective temperature, all from Bordé et al. (2002; based on Cohen et al. 1999).

Star	Sp. type	K	Θ_{UD}	$\sigma(\Theta)$	T_{eff}
56 Aql	K5 III	1.76	2.45	0.028	4046
31 Ori	K5 III	0.90	3.56	0.057	4046
58 Hya	K2.5 IIIb	1.13	3.13	0.035	4318
66 Aql	K5 III	1.76	2.37	0.030	4046
70 Aql	K5 II	1.21	3.18	0.037	4064
θ Cen	K0-IIIb	−0.26	5.32	0.058	4656
ϕ^1 Aqr	K1-III	1.79	2.18	0.025	4508
λ Gru	K3 III	1.44	2.64	0.030	4256
λ Sgr	K1 IIIb	0.40	4.13	0.047	4508
π^2 Ori	K0 IIIb	1.69	2.14	0.023	4656
χ Phe	K5 III	1.52	2.69	0.032	4046
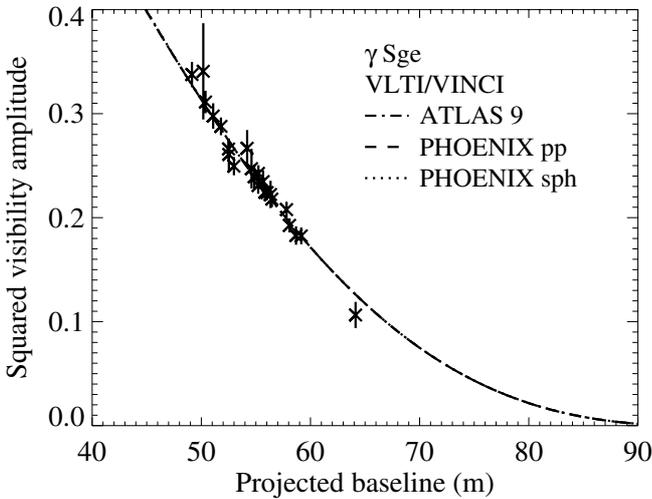
Fig. 8. Measured γ Sagittae squared visibility amplitudes obtained with VLTI/VINCI in June to September 2002, together with the synthetic visibility curves of the best fitting models.

of the integral was then performed using the Romberg method. Numerical results were checked against analytical results for UD and FDD cases, and the resulting visibility function for other cases was inspected for irregularities.

Broad-band visibility values integrated over the bandpasses of our NPOI spectral channels and VINCI sensitivity function are calculated using Eqs. (3) and (4), respectively.

4.3. Calculation of best fitting angular diameters

We calculate the best fitting limb-darkened (0% intensity) angular diameter Θ_{LD} as described above for each of these three model atmospheres (plane-parallel ATLAS 9, plane-parallel PHOENIX, spherical PHOENIX models) and for each of our two data sets (NPOI and VLTI/VINCI). For each model fit, we treat Θ_{LD} as the only free parameter, and use all NPOI visibility data (squared visibility amplitudes, triple amplitudes, and closure phases), a total of 644 data points, simultaneously. The fit is a standard least-square fit, and optimises the total χ^2 value of all 644 NPOI data points.

As discussed in Sect. 3.4 of Paper II, models based on plane-parallel geometry are optically thick from all viewing angles, the intensity steeply dropping to 0 directly at the stellar limb.

Table 3. Details of our VLTI/VINCI observations of γ Sagittae (date and time of observation, spatial frequency, azimuth angle of the projected baseline (E of N)), together with the measured squared visibility amplitudes and their errors. The last column denotes the number of successfully processed interferograms for each series. The effective wavelength for our γ Sagittae observations is ~2.19 μm. For each date of observation, we list the equivalent uniform disc (UD) diameter obtained from only the data of the specific night. Using all data together, we obtain an equivalent UD diameter of $\Theta_{UD} = 5.93 \pm 0.02$ mas, or an equivalent FDD diameter of $\Theta_{FDD} = 6.69 \pm 0.02$ mas.

UT	Sp. freq [1/″]	az [deg]	V^2	σ_{V^2}	#
		28 June 2002, $\Theta_{UD} = 5.91 \pm 0.03$ mas			
05:16:57	131.14	136.63	1.825e−01	8.074e−03	161
05:22:40	130.08	136.65	1.828e−01	8.852e−03	152
05:32:34	128.15	136.73	2.077e−01	7.578e−03	172
06:44:22	111.69	139.42	3.112e−01	1.079e−02	80
		8 July 2002, $\Theta_{UD} = 5.89 \pm 0.04$ mas			
05:12:10	124.21	137.05	2.241e−01	7.199e−03	397
05:20:13	122.44	137.27	2.426e−01	7.846e−03	418
		11 July 2002, $\Theta_{UD} = 5.98 \pm 0.04$ mas			
03:06:45	142.16	138.28	1.064e−01	1.256e−02	55
05:29:49	117.47	138.08	2.495e−01	8.775e−03	69
05:34:22	116.38	138.31	2.660e−01	9.929e−03	207
05:40:41	114.83	138.64	2.878e−01	8.524e−03	297
05:47:01	113.25	139.02	2.977e−01	1.228e−02	198
		15 July 2002, $\Theta_{UD} = 5.94 \pm 0.05$ mas			
04:22:40	128.76	136.70	1.926e−01	6.824e−03	90
04:41:27	124.90	136.98	2.223e−01	1.315e−02	139
		8 August 2002, $\Theta_{UD} = 5.92 \pm 0.03$ mas			
03:05:49	125.17	136.95	2.179e−01	7.678e−03	469
03:12:20	123.77	137.10	2.244e−01	9.005e−03	436
03:18:34	122.39	137.27	2.309e−01	7.979e−03	468
03:24:34	121.03	137.47	2.471e−01	1.901e−02	178
04:13:56	108.94	140.21	3.376e−01	1.212e−02	423
		12 September 2002, $\Theta_{UD} = 5.99 \pm 0.11$ mas			
01:26:22	116.44	138.29	2.607e−01	1.547e−02	190
01:47:17	111.24	139.54	3.407e−01	4.631e−02	105
		18 September 2002, $\Theta_{UD} = 5.88 \pm 0.05$ mas			
00:32:53	123.38	137.15	2.347e−01	1.081e−02	428
00:40:53	121.59	137.39	2.393e−01	1.177e−02	407
00:47:14	120.14	137.61	2.667e−01	1.751e−02	210

Table 4. Fit results of our VINCI data to UD and FDD models.

Model	Diameter	χ^2_ν
UD	$\Theta_{UD} = 5.93 \pm 0.02$ mas	0.63
FDD	$\Theta_{FDD} = 6.69 \pm 0.02$ mas	0.63

A plane-parallel model has, by definition, an atmosphere with an negligible thickness relative to the stellar radius. Therefore, since any depth in such an atmosphere has a radius effectively equal to the stellar radius, a Rosseland diameter Θ_{Ross} in such a geometry is equivalent to the limb-darkened (or 0% intensity) diameter Θ_{LD}.

Intensity profiles based on atmosphere models with spherical geometry, exhibit an inflection point and steepest decrease at radii smaller than the outermost model radius. The Rosseland mean optical depth increases slowly for increasing angles μ. Here, the ratio of the Rosseland diameter Θ_{Ross} and the 0% intensity diameter Θ_{LD} differs from unity, and this ratio $C_{Ross/LD}$ is model-dependent and can be derived from the structure of the model atmosphere. This value depends on the definition of the outermost radius R_0 of the model. R_0 of the spherical PHOENIX model used here is given by the standard boundary

conditions, which are a continuum optical depth of 1e–6 at 1.2 μm and an outer gas pressure of 1e–4 dynes/cm^2 (see Paper II).

4.4. Results and discussion

Results. Table 5 shows, separately for our NPOI and VINCI data sets, the resulting best-fitting angular diameter values based on the different considered model atmospheres, together with the corresponding χ_ν^2 values. For the spherical model atmospheres, the 0% intensity diameter Θ_{LD} is transformed to the Rosseland diameter Θ_{Ross} as described above.

The corresponding synthetic visibility data are compared to the measured data in Figs. 3 to 7 for our NPOI data set and in Fig. 8 for our VLTI/VINCI data set.

Best-fitting angular diameters. Based on the plane-parallel `ATLAS 9` model and our NPOI data, we reproduce the limb-darkened diameter $\Theta_{LD} = 6.18 \pm 0.06$ mas from Paper I, despite the greater usable wavelength range and higher precision of the current NPOI data. The error includes an adopted 1% systematic error due to the NPOI wavelength calibration (the formal error is 0.004 mas). The VLTI/VINCI diameter for this model atmosphere of $\Theta_{LD} = 6.08 \pm 0.02$ mas is not well consistent with the NPOI diameter ($\approx 2\sigma$ difference).

The plane-parallel `PHOENIX` model leaves the near-infrared VLTI/VINCI diameter quasi unchanged (6.09 mas compared to 6.08 mas) with respect to the plane-parallel `ATLAS` model, while it results in a smaller (by $\approx 1\sigma$) visual NPOI diameter compared to the `ATLAS` model. A comparison of these models' temperature structures reveals that the `ATLAS` model exhibits a steeper temperature gradient relative to the plane-parallel `PHOENIX` near Rosseland optical depth unity. This steeper gradient leads to stronger limb darkening at NPOI wavelengths and consequently a larger best angular diameter. The shallower temperature gradient of the plane-parallel `PHOENIX` model leads to a better agreement between the NPOI and VLTI/VINCI diameters.

Finally, the spherical `PHOENIX` model leads to a Rosseland angular diameter of $\Theta_{Ross} = 6.02 \pm 0.06$ mas for the NPOI data set and $\Theta_{Ross} = 6.06 \pm 0.02$ mas for the VLTI/VINCI data set. The larger best-fit diameters for the plane-parallel `PHOENIX` model compared to the spherical `PHOENIX` model appears to be due to model geometry. The agreement of NPOI and VLTI/VINCI data sets within their 1σ error bars gives confidence in both, the atmosphere models and the accuracy of the results from NPOI and VLTI/VINCI. The weighted mean of the NPOI and VLTI/VINCI results is $\Theta_{Ross} = 6.06 \pm 0.02$ mas.

Shape of the visibility function. The measured and model-predicted visibility functions are generally consistent. However, the obtained reduced χ_ν^2 values for the NPOI data between 2.2 and 2.4 are above unity, as would be expected for a perfect match. This indicates differences at the 2σ level between observed visibility data and the model predictions.

These differences are most evident in (1) a lower second maximum of the measured visibility function with respect to the model prediction on the EW baseline (Fig. 3), and (2) a flattened measured visibility function with respect to the model predictions at the blue end on the CW baseline (Fig. 4). It is not yet clear if and by how far these deviations of measured and synthetic visibility functions indicate different details of the limb-darkening effect at visual spectral channels, or if they are caused

by additional calibration uncertainties that are not included in the error bars. In particular the flattening of the measured visibility function at the bluest spectral channels on the CW baseline can most likely be explained by additional calibration uncertainties of our NPOI data, as the instrumental transfer function for these data exhibits a drop which may not be fully compensated.

The obtained diameter values in Table 5 are not affected by possible calibration uncertainties since the best-fitting diameter for any given model atmosphere is mostly constrained by the position of the first minimum and the global shape of the visibility curve.

At optical wavelengths including all our NPOI spectral channels, TiO absorption bands are very important for the modelling of atmospheres of cool giants. It has been shown that the use of different line list combinations of TiO and H_2O leads to significantly different model structures and spectra, in particular in the optical where TiO bands are important (Allard et al. 2000). A possible explanation for differences between our visibility data and the model predictions could thus also be mismatching opacity tables for the TiO bands and/or a mismatching spatial structure of the layers where TiO molecules reside.

In order to estimate the effect of a lower model strength of the limb-darkening effect on the obtained diameter value, we used a spherical `PHOENIX` model with $T_{eff} = 3500$ K instead of our favourite model with $T_{eff} = 3750$ K (other parameters unchanged). The height of the second maximum of the visibility function at a wavelength of 600 nm is reduced from ≈ 0.0085 (see the lower right panel of Fig. 3) to ≈ 0.0070. The obtained best-fitting diameter value for the NPOI data set changes from $\Theta_{Ross} = 6.02 \pm 0.06$ mas to $\Theta_{Ross} = 6.03 \pm 0.06$ mas, and is unchanged for the VLTI/VINCI data set. This shows that an imperfect modelling of the strength of the limb-darkening effect within our uncertainties does not have a significant effect on our obtained diameter values for γ Sge.

Model atmosphere fluxes. Figure 9 shows the measured flux of γ Sge from Alekseeva et al. (1997) in the wavelength range from 0.4–1.0 μm, i.e. covering the NPOI range used in this paper. Also shown are the predictions by the model atmospheres with parameters listed in Table 5. The limb-darkened 0% diameter values Θ_{LD} derived from the fit to the interferometric data were used to scale the model SEDs. The spectral resolution of the model SEDs is convolved to the resolution of the data used, i.e. to 10 nm. The model-predicted flux curves based on the three considered models are well consistent with the general shape of the measured flux, while the detailed description of the spectral bands and features differs between the different models and the measured values. These differences can most likely be explained by the treatment of TiO absorption lines which are important for the visual wavelength range and difficult to model (Allard et al. 2000), as mentioned in the paragraph above.

Deviations from circular symmetry. Differences between data and models are also observed for the closure phases (Fig. 7). The observed smooth variation of the closure phases from 0 to π instead of the expected instantaneous flip may indicate a small deviation from spherical symmetry as already mentioned in Paper I. As our maximum spatial resolution reaches 2.7 mas, and the stellar disc has a size of $\Theta_{Ross} = 6.06$ mas, the stellar disc is well resolved with 2.2 resolution elements across the disc. As a result, our data is sensitive to small deviations of circular symmetry. Such a deviation can in principle be caused by surface features such as spots, an asymmetric shape of the photosphere

Table 5. Results for the fit of `ATLAS 9` and `PHOENIX` model atmospheres to our interferometric VLTI/VINCI and NPOI data sets of γ Sagittae.

Model atmosphere	NPOI (526 nm to 852 nm)	VLTI/VINCI (2190 nm)
`ATLAS 9`, plane-parallel, $T_{\rm eff} = 3750$ K, $\log g = 1.0$	$\Theta_{\rm LD} = 6.18 \pm 0.06$ mas	$\Theta_{\rm LD} = 6.08 \pm 0.02$ mas
	$\chi^2_\nu = 2.2$	$\chi^2_\nu = 0.6$
`PHOENIX`, plane-parallel, $T_{\rm eff} = 3750$ K, $\log g = 1.0$	$\Theta_{\rm LD} = 6.11 \pm 0.06$ mas	$\Theta_{\rm LD} = 6.09 \pm 0.02$ mas
	$\chi^2_\nu = 2.3$	$\chi^2_\nu = 0.6$
`PHOENIX`, spherical, $T_{\rm eff} = 3750$ K, $\log g = 1.0$, $M = 1.3\ M_\odot$	$\Theta_{\rm LD} = 6.30 \pm 0.06$ mas	$\Theta_{\rm LD} = 6.34 \pm 0.02$ mas
	$\chi^2_\nu = 2.4$	$\chi^2_\nu = 0.6$
	$\Theta_{\rm Ross} = 6.02 \pm 0.06$ mas	$\Theta_{\rm Ross} = 6.06 \pm 0.02$ mas
	$\overline{\Theta_{\rm Ross} = 6.06 \pm 0.02 \text{ mas}}$	
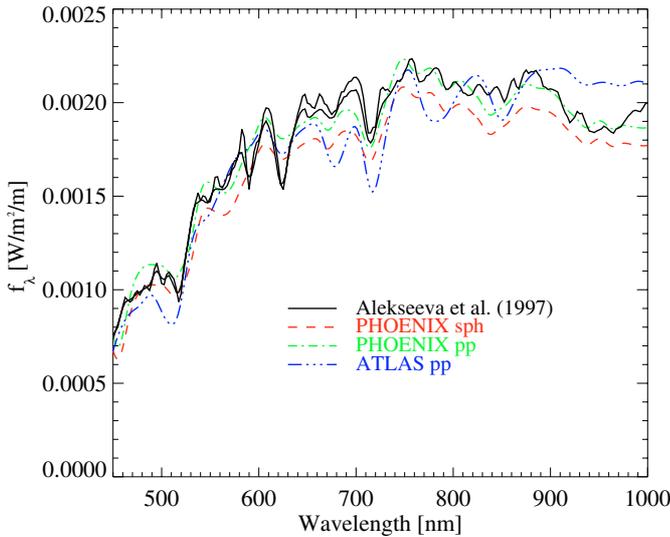
Fig. 9. Flux of γ Sge from Alekseeva et al. (1997) in the wavelength range of our NPOI observations, compared to the model atmosphere predictions with model parameters listed in Table 5. The limb-darkened 0% diameter values $\Theta_{\rm LD}$ derived from the fit to the interferometric data were used to scale the model SEDs. The spectral resolution of the model SEDs is convolved to the resolution of the data used, i.e. to 10 nm.

or of more extended (molecular) layers, or a faint unknown companion. Our target γ Sge shows a relatively high photospheric pressure scale height of $H_{\rm P0} = R_{\rm gas} T_{\rm eff}/g \approx 0.006\ R_\star$. Relatively large-scale ($\approx 0.06\ R_\star$) surface inhomogeneities caused by convection could thus be expected (cf. Freytag et al. 1997).

Spherical versus plane-parallel model geometry. The synthetic visibility data based on the same `PHOENIX` models that solely differ by spherical versus plane-parallel model geometry are virtually identical (Figs. 3–7). Thus, the model geometry has no noticeable effect on the shape of the visibility and can not be constrained by our visibility data. However, the derived angular diameter values differ by 1.5% for the visual NPOI data and by 0.5% for the near-infrared VLTI/VINCI data. The spherical geometry allows us to more precisely define the stellar Rosseland radius with respect to the outermost model layer, and is thus more reliable than the angular diameter obtained from the plane-parallel model. As already noticed in Paper II for the M4 giant ψ Phe, the 0% intensity (LD) diameter based on a plane-parallel model seems to somewhat overestimate the stellar diameter with respect to the Rosseland diameter based

Table 6. Revised fundamental parameters of the M0 giant γ Sagittae based on the analysis of this paper. For the details of the calculation, see the text.

Parameter	Value
Rosseland angular diameter	$\Theta_{\rm Ross} = 6.06 \pm 0.02$ mas
Rosseland linear radius	$R_{\rm Ross} = 55 \pm 4\ R_\odot$
Bolometric flux	$f_{\rm bol} = (2.57 \pm 0.13) \times 10^{-9}$ W/m^2
Effective temperature	$T_{\rm eff} = 3805 \pm 55$ K
Luminosity	$\log L/L_\odot = 2.75 \pm 0.08$
Mass	$M = 1.4 \pm 0.4\ M_\odot$
Surface gravity	$\log g = 1.1 \pm 0.2$

on a spherical model. Our present results indicate a wavelength-dependent amount of this overestimation.

5. Summary and conclusions

We have compared our visual γ Sagittae NPOI visibility data for 19 spectral channels with central wavelengths between 526 nm to 852 nm as well as our near-infrared K-band VLTI/VINCI visibility data with effective wavelength 2.19 μm to a plane-parallel `ATLAS 9`, a plane-parallel `PHOENIX`, and a spherical `PHOENIX` model atmosphere. The stellar parameters effective temperature $T_{\rm eff}$, surface gravity $\log g$, and M of the model atmospheres used were fixed a-priori based on previous information on this star.

The spherical geometry of the `PHOENIX` model enables us to precisely define the Rosseland radius of the star with respect to the outermost model layer and thus the 0% intensity diameter. This model leads to consistent Rosseland angular diameters for our NPOI and VLTI/VINCI data sets. This agreement increases the confidence in the model atmosphere predictions from optical to near-infrared wavelengths as well as in the calibration and accuracy of both interferometric facilities. In addition, the consistent angular diameter derived from our VLTI/VINCI data on a night-by-night basis over a total range of about 2 months increases confidence in the given calibration uncertainties.

The Rosseland angular diameter of γ Sagittae of $\Theta_{\rm Ross} = 6.06 \pm 0.02$ mas, based on the comparison of our NPOI and VLTI/VINCI data to the spherical `PHOENIX` model, corresponds to a Rosseland linear radius of $R_{\rm Ross} = 55 \pm 4\ R_\odot$, derived with the Hipparcos parallax of $\pi = 11.90 \pm 0.71$ mas. The error of the Rosseland linear radius is dominated by the uncertainty of the parallax, not by the precision of our interferometric measurement. With the bolometric flux $f_{\rm bol} = (2.57 \pm 0.13) \times 10^{-9}$ W/m^2 (Sect. 1) and the Rosseland angular diameter, the effective temperature is constrained to $T_{\rm eff} = 3805 \pm 55$ K. Again, the major

contribution to this error originates from the uncertainty in f_{bol} and not from our interferometric measurement. The Rosseland linear radius and T_{eff} result in a luminosity of $\log L/L_\odot = 2.75 \pm 0.08$. Placing γ Sagittae on the Hertzsprung Russel diagram using these values, and comparing to stellar evolutionary tracks by Girardi et al. (2000) as in Paper II (Fig. 1 of Paper II) we can estimate a mass of $M = 1.4 \pm 0.4\ M_\odot$, and thus a surface gravity of $\log g = 1.1 \pm 0.2$. Table 6 summarises our revised values of γ Sagittae's fundamental parameters.

The closure phases show a smooth transition from 0 to π rather than a sharp flip, which could be due to a small deviation from circular symmetry of the well resolved stellar disc due to surface features such as spots, an asymmetric extended molecular layer, or a faint companion.

References

Alekseeva, G. A., Arkharov, A. A., Galkin, V. D., et al. 1997, VizieR Online Data Catalog, 3201, 0
Allard, F., Hauschildt, P. H., & Schwenke, D. 2000, ApJ, 540, 1005
Armstrong, J. T., Mozurkewich, D., Rickard, L. J., et al. 1998, ApJ, 496, 550
Alonso, A., Arribas, S., & Martínez-Roger, C. 1999, A&AS, 139, 335
Aufdenberg, J. P., & Hauschildt, P. H. 2003, Proc. SPIE, 4838, 193
Aufdenberg, J. P., Ludwig, H.-G., & Kervella, P. 2005, ApJ, 633, 424
Bordé, P., Coudé du Foresto, V., Chagnon, G., & Perrin, G. 2002, A&A, 393, 183
Burns, D., Baldwin, J. E., Boysen, R. C., et al. 1997, MNRAS, 290, L11
Cohen, M., Walker, R. G., Carter, B., et al. 1999, AJ, 117, 1864
Davis, J., Tango, W. J., & Booth, A. J. 2000, MNRAS, 318, 387
Fedele, D., Wittkowski, M., Paresce, F., et al. 2005, A&A, 431, 1019
Freytag, B., Holweger, H., Steffen, M., & Ludwig, H.-G. 1997, Science with the VLT Interferometer, 316
Girardi, L., Bressan, A., Bertelli, G., & Chiosi, C. 2000, A&AS, 141, 371
Glindemann, A., Algomedo, J., Amestica, R., et al. 2003, Ap&SS, 286, 35
Hajian, A. R., Armstrong, J. T., Hummel, C. A., et al. 1998, ApJ, 496, 484
Hanbury Brown, R., Davis, J., Lake, R. J. W., & Thompson, R. J. 1974, MNRAS, 167, 475
Hauschildt, P. H., Allard, F., Ferguson, J., Baron, E., & Alexander, D. R. 1999, ApJ, 525, 871
Hestroffer, D. 1997, A&A, 327, 199
Hofmann, K.-H., & Scholz, M. 1998, A&A, 335, 637
Hofmann, K.-H., Scholz, M., & Wood, P. R. 1998, A&A, 339, 846
Hummel, C. A., Mozurkewich, D., Armstrong, et al. 1998, AJ, 116, 2536
Hummel, C. A., Mozurkewich, D., Benson, J. A., & Wittkowski, M. 2003, Proc. SPIE, 4838, 1107
Ireland, M. J., & Scholz, M. 2006, MNRAS, 278
Ireland, M. J., Scholz, M., & Wood, P. R. 2004, MNRAS, 352, 318
Jacob, A. P., & Scholz, M. 2002, MNRAS, 336, 1377
Johnson, H. L., & Mitchell, R. I. 1975, Rev. Mex. Astron. Astrofis., 1, 299
Keenan, P. C., & McNeil, R. C. 1989, ApJS, 71, 245
Kervella, P., Gitton, P., Ségransan, D., et al. 2003, Proc. SPIE, 4838, 858
Kervella, P., Ségransan, D., & Coudé du Foresto, V. 2004, A&A, 425, 1161
Kurucz, R. 1993, Limbdarkening for 2 km s⁻¹ grid (No. 13): [+0.0] to [−5.0]. Kurucz CD-ROM No. 17. Cambridge, Mass.: Smithsonian Astrophysical Observatory
Morgan, W. W., & Keenan, P. C. 1973, ARA&A, 11, 29
Mozurkewich, D., Johnston, K. J., Simon, R. S., et al. 1991, AJ, 101, 2207
Mozurkewich, D., Armstrong, J. T., Hindsley, R. B., et al. 2003, AJ, 126, 2502
Ohnaka, K. 2004a, A&A, 424, 1011
Ohnaka, K. 2004b, A&A, 421, 1149
Ohnaka, K., Bergeat, J., Driebe, T., et al. 2005, A&A, 429, 1057
Perrin, G., Ridgway, S. T., Mennesson, B., et al. 2004, A&A, 426, 279
Perrin, G., Ridgway, S. T., Verhoelst, T., et al. 2005, A&A, 436, 317
Perryman, M. A. C., & ESA 1997, The Hipparcos and Tycho catalogues (Noordwijk, Netherlands: ESA Publications Division), ESA SP Ser., 1200
Peterson, D. M., Hummel, C. A., Pauls, T. A., et al. 2006a, ApJ, 636, 1087
Peterson, D. M., Hummel, C. A., Pauls, T. A., et al. 2006b, Nature, 440, 896
Quirrenbach, A., Mozurkewich, D., Buscher, D. F., Hummel, C. A., & Armstrong, J. T. 1996, A&A, 312, 160
Samus, N. N., Durlevich, O. V., et al. 2004, VizieR Online Data Catalog, 2250, 0
Scholz, M. 1985, A&A, 145, 251
Scholz, M. 1998, Fundamental Stellar Properties, IAU Symp., 189, 51
Scholz, M. 2001, MNRAS, 321, 347
Shao, M., Colavita, M. M., Hines, B. E., et al. 1988, A&A, 193, 357
Tej, A., Lançon, A., Scholz, M., & Wood, P. R. 2003, A&A, 412, 481
Wittkowski, M., Hummel, C. A., Johnston, K. J., et al. 2001, A&A, 377, 981 (Paper I)
Wittkowski, M., Aufdenberg, J. P., & Kervella, P. 2004, A&A, 413, 711 (Paper II)
Woodruff, H. C., Eberhardt, M., Driebe, T., et al. 2004, A&A, 421, 703